

# Generator coordinate method for hypernuclear spectroscopy with a covariant density functional

H. Mei,<sup>1,2</sup> K. Hagino,<sup>1,3,4</sup> and J. M. Yao <sup>\*1,2</sup>

<sup>1</sup>*Department of Physics, Tohoku University, Sendai 980-8578, Japan*

<sup>2</sup>*School of Physical Science and Technology, Southwest University, Chongqing 400715, China*

<sup>3</sup>*Research Center for Electron Photon Science, Tohoku University, 1-2-1 Mikamine, Sendai 982-0826, Japan*

<sup>4</sup>*National Astronomical Observatory of Japan, 2-21-1 Osawa, Mitaka, Tokyo 181-8588, Japan*

We apply the generator coordinate method (GCM) to single- $\Lambda$  hypernuclei in order to discuss the spectra of hypernuclear low-lying states. To this end, we use the same relativistic point-coupling energy functional both for the mean-field and the beyond-mean-field calculations. This relativistic GCM approach provides a unified description of low-lying states in ordinary nuclei and in hypernuclei, and is thus suitable for studying the  $\Lambda$  impurity effect. We carry out an illustrative calculation for the low-lying spectrum of  $^{21}_{\Lambda}\text{Ne}$ , in which the interplay between the hypernuclear collective excitations and the single-particle excitations of the unpaired  $\Lambda$  hyperon is taken into account in a full microscopic manner.

PACS numbers: 21.80.+a, 21.60.Jz, 23.20.-g, 21.10.-k

In the past decades, many high-resolution  $\gamma$ -ray spectroscopy experiments have been carried out for  $\Lambda$  hypernuclei. The experimental data on energy spectra and electric multipole transition strengths have been accumulated, providing rich information on a hyperon-nucleon interaction in the nuclear medium as well as the impurity effect of the  $\Lambda$  particle on the structure of atomic nuclei [1, 2]. It is noteworthy that the next-generation facility J-PARC has already been in operation [3], opening up a new opportunity to perform high precision hypernuclear  $\gamma$ -ray spectroscopy studies. These experiments will shed light on low-lying states of hypernuclei, especially those of medium and heavy hypernuclei.

From the theoretical side, the hypernuclear low-lying states have been studied mainly with a shell model [4–6] and with a cluster and few-body models [7–13]. In recent years, several other methods have also been developed for hypernuclear spectroscopy, including an ab-initio method [14], the antisymmetrized molecular dynamics (AMD) [15–17], and the microscopic particle-rotor model based on the covariant density functional theory [18, 19]. The angular momentum projection (but with the scheme of variation-before-projection) for the total hypernuclear wave function has also been carried out with the Skyrme density functional [20], even though the important effect of configuration mixing was not taken into account.

In this paper, we propose a generator coordinate method (GCM) for the whole hypernucleus based on a relativistic energy density functional. To this end, we superpose a set of hypernuclear mean-field states projected onto the states with good quantum numbers of the particle number and the angular momentum. Such configura-

tion mixing effect was missing in Ref. [20], and thus our calculation serves as one of the most advanced beyond-mean-field methods for the spectroscopy of hypernuclear low-lying states. In contrast to the microscopic particle-rotor model developed in Refs. [18, 19], where the GCM calculation is carried out only for the core nucleus, all the nucleons and the hyperon are treated on the same footing in the present approach. As we shall discuss, these two methods are in fact complementary to each other, both from the physics point of view and from the numerical point of view.

Our aim in this paper is to describe low-lying states of odd-mass  $\Lambda$  hypernuclei which consist of a  $\Lambda$  particle and an even-even nuclear core. In contrast to the unpaired nucleon in ordinary odd-mass nuclei, the unpaired  $\Lambda$  hyperon in the hypernucleus is free from the Pauli exclusion principle from the nucleons inside the nuclear core. In principle, the  $\Lambda$  hyperon can thus occupy any bound hyperon orbital, providing a unique platform to study the interplay of the individual single-particle motion of the hyperon with the nuclear collective motions. The wave function of these hypernuclear states are constructed as a superposition of quantum-number projected hypernuclear reference states with different quadrupole deformation  $\beta$ ,

$$|\Psi_{n\alpha}^{JM}\rangle = \sum_{\beta} f_{n\alpha}^J(\beta) \hat{P}_{MK}^J \hat{P}^N \hat{P}^Z |\Phi_n^{(N\Lambda)}(\beta)\rangle, \quad (1)$$

where the index  $n$  refers to a different hyperon orbital state, and the index  $\alpha$  labels the quantum numbers of the state other than the angular momentum. For simplicity, we take the adiabatic approximation and do not mix different  $n$  in the total wave function,  $|\Psi_{n\alpha}^{JM}\rangle$ .

In Eq. (1), the mean-field states  $|\Phi_n^{(N\Lambda)}(\beta)\rangle$ , severing as nonorthonormal basis, are generated with deformation constrained relativistic mean-field (RMF) calculations for  $\Lambda$  hypernuclei [21–23]. Since the hyperon and the nucleons are not mixed, the mean-field states can be

---

\*Present address: Department of Physics and Astronomy, University of North Carolina, Chapel Hill, North Carolina 27516-3255, USA

decomposed as

$$|\Phi_n^{(N\Lambda)}(\beta)\rangle = |\Phi^N(\beta)\rangle \otimes |\varphi_n^\Lambda(\beta)\rangle, \quad (2)$$

where  $|\Phi^N(\beta)\rangle$  and  $|\varphi_n^\Lambda(\beta)\rangle$  are the mean-field wave functions for the nuclear core and the hyperon, respectively. With this wave function, the deformation parameter  $\beta$  is related to the mass quadrupole moment of the whole hypernucleus  ${}^\Lambda_Z$  as

$$\beta = \frac{4\pi}{3AR^2} \langle \Phi_n^{(N\Lambda)}(\beta) | r^2 Y_{20} | \Phi_n^{(N\Lambda)}(\beta) \rangle, \quad (3)$$

with  $R = 1.2 \times A_c^{1/3}$  fm,  $A_c = A - 1$  being the mass number of the core nucleus. In this paper, in order to reduce the computation burden, we restrict all the reference states to be axially deformed. The mean-field states  $|\Phi_n^{(N\Lambda)}(\beta)\rangle$  are then projected onto states with good quantum numbers with the operators  $\hat{P}^N$  ( $\hat{P}^Z$ ), and  $\hat{P}_{MK}^J$ , which project out the component with good neutron (proton) numbers and the angular momentum [24]. Here, the total angular momentum  $J$  is a half-integer number and  $K$  is its projection on the  $z$ -axis in the body-fixed frame. We assume that all the nucleons fill time-reversal states and thus do not contribute to the total angular momentum along the symmetric axis. In this case, the  $K$  quantum number is identical to  $\Omega$ , that is, the component of the angular momentum of the hyperon along the  $z$ -axis, and thus can be adopted to characterize the wave function  $|\varphi_n^\Lambda(\beta)\rangle$ . From the mean-field states with the hyperon in a  $\Omega^\pi$  configuration, the angular momentum  $J$  takes the value of  $|\Omega|, |\Omega| + 1, \dots$ . Notice that, in the angular momentum projection, the integrals over the two Euler angles  $\phi$  and  $\psi$  can be performed analytically because of the axial symmetry.

The weight function  $f_{n\alpha}^J(\beta)$  in the GCM states given by Eq. (1) is determined by the variational principle, which leads to the Hill-Wheeler-Griffin (HWG) equation,

$$\sum_{\beta'} [\mathcal{H}_n^J(\beta, \beta') - E_{n\alpha}^J \mathcal{N}_n^J(\beta, \beta')] f_{n\alpha}^J(\beta') = 0, \quad (4)$$

where the norm kernel  $\mathcal{N}_n^J(\beta, \beta')$  and the Hamiltonian kernel  $\mathcal{H}_n^J(\beta, \beta')$  are defined as

$$\mathcal{O}_n^J(\beta, \beta') \equiv \langle \Phi_n^{(N\Lambda)}(\beta) | \hat{O} \hat{P}_{KK}^J \hat{P}^N \hat{P}^Z | \Phi_n^{(N\Lambda)}(\beta') \rangle, \quad (5)$$

with  $\hat{O} = 1$  and  $\hat{O} = \hat{H}$ , respectively. The solution of the HWG equation (4) provides the energy  $E_{n\alpha}^J$  and the weight function  $f_{n\alpha}^J(\beta)$  for each of the low-lying states of hypernuclei. In the actual calculations, we evaluate the Hamiltonian overlap with the mixed density prescription [25, 26].

As an illustration of the method, we apply the GCM approach to  ${}^{21}_\Lambda\text{Ne}$ . We first generate a set of hypernuclear reference states  $|\Phi_n^{(N\Lambda)}(\beta)\rangle$ , by putting the hyperon on the four lowest single-particle states with  $\Omega^\pi = 1/2_1^+, 1/2_1^-, 3/2_1^-,$  and  $1/2_2^-$ . To this end, we perform

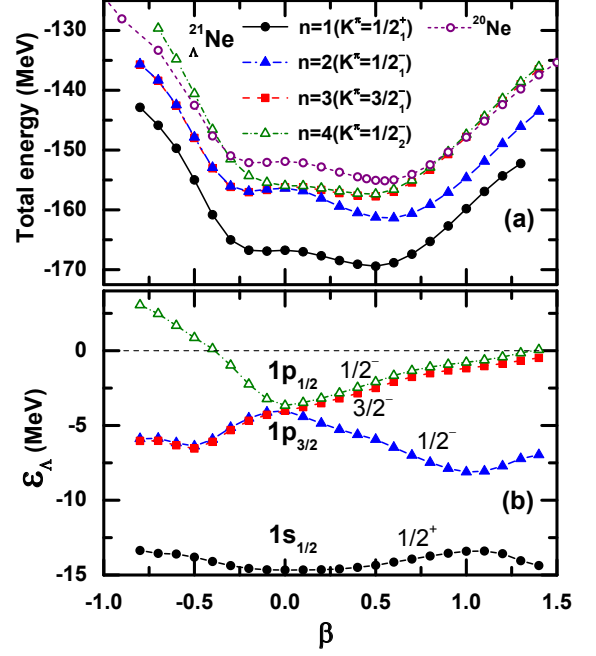


FIG. 1: (Color online)(a) The total energy curves for  ${}^{21}_\Lambda\text{Ne}$  obtained in the mean-field approximation as a function of quadrupole deformation  $\beta$ . These are calculated by putting the  $\Lambda$  hyperon in different single-particle orbitals shown in the lower panel. For comparison, the energy curve for the core nucleus  ${}^{20}\text{Ne}$  is also plotted. (b) The single-particle energies of the  $\Lambda$  hyperon in  ${}^{21}_\Lambda\text{Ne}$  as a function of quadrupole deformation. These are labeled with the  $\Omega^\pi$  number, that is the projection of the angular momentum onto the  $z$ -axis in the body fixed frame.

the deformation constrained RMF+BCS calculation using the PC-F1 force [27] for the nucleon-nucleon interaction and the PCY-S2 force [28] for the nucleon- $\Lambda$  interaction. A density-independent  $\delta$  force is used in the pairing channel for the nucleons, supplemented with an energy-dependent cutoff [29]. The Dirac equations are solved by expanding the Dirac spinors with harmonic oscillator wave functions with 10 oscillator shells. See Refs. [23, 30] for numerical details.

Figure 1(a) shows the mean-field energies for the reference states so obtained as a function of deformation parameter  $\beta$ . One can see that the energies for the three negative-parity configurations (that is,  $\Omega^\pi = 1/2_1^-, 3/2_1^-,$  and  $1/2_2^-$ ), corresponding to the hyperon occupying the three “ $p$ -orbital” states, are close to each other at  $\beta = 0$  due to a weak hyperon spin-orbit interaction, and are well separated from the energy of the positive parity configuration ( $\Omega^\pi = 1/2_1^+$ ), which corresponds to the hyperon occupying the “ $s$ -orbital” state. The energy difference between the positive- and the negative-parity energy configurations at  $\beta = 0$  is about 10.4 MeV, which is consistent with the  $2/3$  of the energy scale  $\hbar\omega = 41A^{-1/3}$  MeV for nucleons. This energy corresponds to the excitation energy of hyperon from the  $s$ -orbital to the  $p$ -orbital.

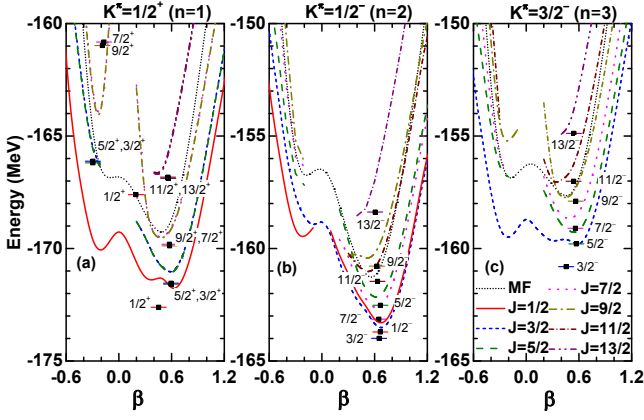


FIG. 2: (Color online) The projected energy curves for  $^{21}_{\Lambda}\text{Ne}$  obtained by putting the  $\Lambda$  hyperon on the three lowest single-particle orbitals labeled by  $\Omega^{\pi}(=K^{\pi})$ . The corresponding mean-field energy curves are also shown for a comparison. The solutions of the GCM calculations are indicated by the squares and the horizontal bars placed at the average deformation.

Moreover, one can also see that the energy minimum appears at  $\beta \sim 0.6$  for  $K^{\pi} = 1/2^{-}$ , which is larger than the deformation of the energy minimum for the  $1/2^{+}$  configuration ( $\beta = 0.49$ ). This is consistent with the findings in Refs. [15, 23] that the hyperon in the “ $p$ -orbital” tends to develop a pronounced energy minima with a larger deformation.

Figure 1(b) shows the Nilsson diagram for the hyperon in  $^{21}_{\Lambda}\text{Ne}$ . The single-particle level with the  $\Omega^{\pi} = 3/2^{-}$  configuration is approximately degenerate with the  $\Omega^{\pi} = 1/2^{-}$  and  $1/2_{2}^{-}$  configurations at the oblate and the prolate sides, respectively. This is a characteristic feature of the Nilsson diagram without the spin-orbit interaction [24], and is responsible for the approximate degeneracy of the corresponding total energy curves shown in Fig. 1(a). We note that the second  $1/2^{-}$  single-particle level becomes unbound on the oblate side with deformation parameter of  $\beta < -0.3$ . In the following discussions, we therefore focus on the hypernuclear states generated by the  $\Lambda$  hyperon occupying the  $\Omega^{\pi} = 1/2_{1}^{+}, 1/2_{1}^{-}$ , and  $3/2_{1}^{-}$  configurations.

The energy curves shown in Fig. 1(a) are the results of the mean-field approximation, in which the reference states are not the eigen-states of the angular momentum and the nucleon numbers. The projected energy curves, after the projection procedures, are obtained by taking the diagonal element of the Hamiltonian and the norm kernels as  $E_n^J(\beta) = \mathcal{H}_n^J(\beta, \beta) / \mathcal{N}_n^J(\beta, \beta)$ . Those energy curves are plotted in Fig. 2 as a function of  $\beta$ . For the  $K^{\pi} = 1/2_{1}^{+}$  configuration shown in Fig. 2(a), the projected energy curves for  $J^{\pi} = 3/2^{+}$  and  $5/2^{+}$  almost overlap with each other, indicating a weak coupling of the  $\Lambda$  hyperon to the nuclear core. This is the case also for the pairs of  $J^{\pi} = (7/2^{+}, 9/2^{+})$  and  $J^{\pi} = (11/2^{+}, 13/2^{+})$ . It is seen that the prolate minimum in the projected

energy curves becomes more pronounced and thus the nuclear shape becomes more stable as the angular momentum increases. Moreover, the energy minimum for the  $J^{\pi} = 1/2^{+}$  energy curve appears at deformation  $\beta = 0.62$ , that is somewhat larger than the deformation at the minimum of the corresponding mean-field curve,  $\beta = 0.49$ , due to the energy gain originated from the angular momentum projection. On the other hand, if one compares it to the projected energy curve for the  $0^{+}$  configuration of  $^{20}\text{Ne}$ , which has a minimum at  $\beta = 0.65$ , one finds that the minimum is slightly shifted towards the spherical configuration both on the oblate and the prolate sides, similarly to the finding of the microscopic particle rotor model [19].

In contrast to the  $J^{\pi} = 1/2^{+}$  configuration, the deformation at the energy minimum for the  $J^{\pi} = 1/2^{-}$  configuration increases to  $\beta = 0.69$  (see Fig. 2(b)). Moreover, for this configuration, the energy difference between the prolate and the oblate minima significantly increases as compared to the  $J^{\pi} = 1/2^{+}$  configuration. For this reason, the collective wave function for the  $J^{\pi} = 1/2^{-}$  state is expected to be more localized on the prolate side than that of the  $J^{\pi} = 1/2^{+}$  state. As a consequence, the average deformation for the  $J^{\pi} = 1/2^{-}$  state is close to the minimum point of the energy curve while that for the  $J^{\pi} = 1/2^{+}$  configuration is shifted towards the oblate side due to a cancellation between the prolate and the oblate contributions (see the filled squares in Fig. 2(a) and 2(b)).

The projected energy curves for the  $K^{\pi} = 3/2_{1}^{-}$  configuration are shown in Fig. 2(c). These are several MeV higher than those for the  $K^{\pi} = 1/2_{1}^{-}$  configuration. Besides, the energy curve for the  $J^{\pi} = 3/2^{-}$  is considerably different from that for the  $J^{\pi} = 5/2^{-}$  configuration, and one would not expect a (quasi-)degeneracy between these two states.

By mixing all the projected mean-field states for each  $K^{\pi}$  configuration, we construct the low-lying states of  $^{20}\text{Ne}$  and  $^{21}_{\Lambda}\text{Ne}$  with the GCM method. The calculated spectra are shown in Fig. 3. One can see that the rotational character of the yrast states of  $^{20}\text{Ne}$  is well reproduced, although the moment of inertia is somewhat overestimated due to the pairing collapse in the reference states for  $\beta > 0.5$ . This problem is expected to be improved by introducing the method of particle-number projection before variation while generating the reference states. The  $\Lambda$  binding energy of  $^{21}_{\Lambda}\text{Ne}$ , defined as the energy difference between the  $0_{1}^{+}$  state of  $^{20}\text{Ne}$  and the  $1/2_{1}^{+}$  state of  $^{21}_{\Lambda}\text{Ne}$ , is calculated to be  $B_{\Lambda} = 14.11$  MeV, which is slightly smaller than the mean-field result of 14.27 MeV.

According to a naive picture of a deformed rotor coupled to a hyperon moving in the deformed potential, one may expect several rotational bands with angular momenta in the order of  $J = |\Omega|, |\Omega| + 1, \dots$  built on top of each single-particle state of  $\Lambda$  hyperon with  $\Omega^{\pi}$ . This picture is indeed realized for the  $K^{\pi} = 3/2^{-}$  band shown in Fig. 3 (d), but is somewhat distorted for the  $K^{\pi} = 1/2^{+}$

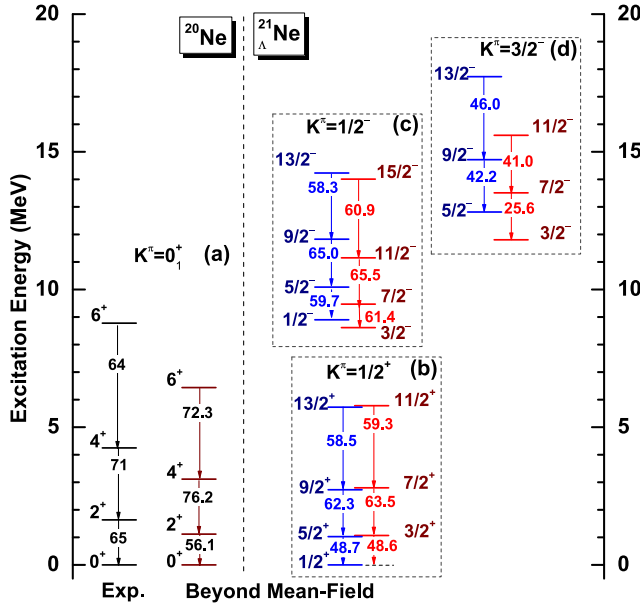


FIG. 3: (Color online) The low-lying excitation spectra of  $^{20}\text{Ne}$  (a) and  $^{21}_{\Lambda}\text{Ne}$  [(b)-(d)] constructed with the GCM approach. The numbers with the arrows indicate the  $E2$  transition strengths, given in units of  $e^2 \text{ fm}^4$ . The experimental data for  $^{20}\text{Ne}$  are taken from Ref. [31].

(b) and  $1/2^-$  (c) bands. In particular, the spin-parity of the bandhead state of the  $K^\pi = 1/2^-$  band is not  $J^\pi = 1/2^-$ , but  $J^\pi = 3/2^-$  due to a large decoupling factor originated from the Coriolis interaction [24]. This effect inverts the energy ordering of the states in the  $K^\pi = 1/2^-$  band by shifting up the states with odd value of  $J+1/2$  and pulling down the states with even values of  $J+1/2$ . As a result, two rotational bands having  $\Delta J = 2$  and with similar electric quadrupole transition strengths are formed. A similar feature has also been found in the microscopic particle-rotor model calculation [19], where the energy displacement between the two bands is, however, much smaller. To be more specific, the energy difference between the  $1/2^-$  and  $3/2^-$  states is less than 40 keV with the microscopic particle-rotor model, while it is 270 keV with the present GCM calculation. We have confirmed that this feature remains the same even if we mix the  $\Omega^\pi = 1/2_1^-$  and  $1/2_2^-$  configurations in the GCM calculations, which alters the excitation energies only by  $\sim 2\%$ .

The  $K^\pi = 1/2^+$  band is mainly formed by the  $\Lambda$  hyperon in the “ $s$ -orbital” coupled to the ground-state band of the nuclear core,  $^{20}\text{Ne}$ . For each core state, except for the ground state, two states appear in this band due to the angular momentum coupling with  $j = 1/2$ , and two rotational series are formed. The energy splitting in the double states is predicted to be small. That is, it is 41.5 keV, 71.2 keV and 53.8 keV, for the doublets ( $3/2^+, 5/2^+$ ), ( $7/2^+, 9/2^+$ ) and ( $11/2^+, 13/2^+$ ), respectively. The magnitude of these energy splittings is comparable to the empirical energy splitting of  $^9_\Lambda\text{Be}$ , for

which the energy of the  $5/2^+$  state is lower than the energy of the state  $3/2^+$  by 43 keV [32]. For the  $E2$  transition strength for  $3/2^+ \rightarrow 1/2^+$  in  $^{21}_{\Lambda}\text{Ne}$ , we find that it is smaller than the  $E2$  strength for  $2^+ \rightarrow 0^+$  in  $^{20}\text{Ne}$  by 13.37%. This implies that the  $\Lambda$  hyperon in the “ $s$ -orbital” decreases the quadrupole collectivity of  $^{20}\text{Ne}$ , which is consistent with the findings in recent theoretical studies [15, 19, 23, 33]. We notice that this is consistent also with the distribution of the collective wave functions, which are shifted towards the small deformation region as compared to those of  $^{20}\text{Ne}$ . On the other hand, the impurity effect for the  $\Lambda$  hyperon in the “ $p$ -orbital” is more difficult to assess, because several configurations are admixed in the wave functions, as has been shown in Ref. [19] with the microscopic particle-rotor model.

In summary, we have applied the generator coordinate method to the spectroscopy of hypernuclear low-lying states. This approach is based on the beyond-mean-field method with the particle number and the angular momentum projections, and takes into account the interplay between the single-particle motion of the  $\Lambda$  hyperon and the hypernuclear collective motion. Using a relativistic point-coupling energy density functional, we have carried out a proof-of-principle calculation for the low-lying states of  $^{21}_{\Lambda}\text{Ne}$ . Our results indicate that the  $\Lambda$  hyperon in the “ $s$ -orbit” couples weakly to the ground-state rotational band of the core nucleus  $^{20}\text{Ne}$ , forming a similar rotational band with almost degenerate doublet states. The  $E2$  transition strength for the  $2^+ \rightarrow 0^+$  transition in  $^{20}\text{Ne}$  is reduced by 13.37% by adding the  $\Lambda$  particle. On the other hand, for the  $\Lambda$  hyperon in the “ $p$ -orbit” the energy difference between similar doublet states is much larger, although the rotational structure of the  $^{20}\text{Ne}$  is still preserved.

We note that for low-lying states of hypernuclei the unpaired hyperon is mainly filled in the deformed states with relatively low orbital angular momenta (that is,  $s$  and  $p$ -like states) and is treated separately in the present GCM approach from the other nucleons. Therefore, the numerical calculation is much simpler than the GCM calculations for ordinary odd-mass nuclei, which has recently been developed based on a Skyrme energy density functional [34]. Moreover, it is straightforward to extend the present method to include more complicated reference states, such as those with triaxial and octupole deformations, even though the numerical complexity will rapidly increase. We note that  $^{20}\text{Ne}$  has prominent negative-parity bands originated from the  $\alpha+^{16}\text{O}$  cluster structure, which would also exist in  $^{21}_{\Lambda}\text{Ne}$ . It would be interesting to study how the octupole deformation in the mean-field states modifies the low-lying states of  $^{21}_{\Lambda}\text{Ne}$ .

The GCM approach presented in this paper is complementary to the microscopic particle-rotor approach which we have developed in the earlier publications [18, 19]. The wave functions for hypernuclear states are expressed in different ways in these approaches. In the microscopic particle rotor model, hypernuclear states are expanded in terms of the low-lying states of the core nucleus, while



they are generated from intrinsic states for the whole system in the present GCM approach. Both methods have advantages and disadvantages. In the microscopic particle-rotor model, the non-adiabatic effects of  $\Lambda$  particle is automatically taken into account, while the  $\Lambda$  particle is restricted to a specific single-particle configuration in the present GCM approach, although this restriction may be easily removed. Another point is that the cut-off of the nuclear core states has to be introduced in the particle-rotor model, while one does not need to worry about it in the GCM approach. From a physics point of view, the microscopic particle-rotor model provides a convenient way to analyze the components of hypernuclear wave function, while the GCM approach offers an intuitive way to study the hypernuclear shape fluctuation as well as the nuclear shape polarization due to the  $\Lambda$  hyperon. From a numerical point of view, the GCM approach is numerically more expensive than the microscopic particle-rotor model, since the norm and the

Hamiltonian kernels have to be constructed for each  $J^\pi$ , whereas it is sufficient to do it only for a limited number of the core states (*e.g.*,  $J^\pi = 0^+, 2^+$ , and  $4^+$ ) in order to construct the whole hypernuclear spectrum with the microscopic particle-rotor model. So far, the microscopic particle-rotor model calculations have been carried out only with a simplified nucleon-hyperon interaction. A comparative study of these two methods using the same nucleon-hyperon effective interaction is an interesting future project, which will deepen our understanding on hypernuclear spectroscopy.

We thank Xian-Rong Zhou for useful discussions. This work was supported in part by the Tohoku University Focused Research Project “Understanding the origins for matters in universe”, JSPS KAKENHI Grant Number 2640263, the NSFC under Grant Nos. 11575148 and 11305134.

- 
- [1] O. Hashimoto and H. Tamura, Prog. Part. Nucl. Phys. **57**, 564 (2006).
  - [2] H. Tamura, Int. J. Mod. Phys. A **24**, 2101 (2009).
  - [3] T.O. Yamamoto *et al.*, Phys. Rev. Lett., in press. arXiv:1508.00376 [nucl-ex].
  - [4] R. H. Dalitz and A. Gal, Ann. Phys. (N.Y.) **116**, 167 (1978).
  - [5] A. Gal, J.M. Soper, and R.H. Dalitz, Ann. Phys. (N.Y.) **63**, 53 (1971).
  - [6] D. J. Millener, Nucl. Phys. **A804**, 84 (2008); **A914**, 109 (2013).
  - [7] T. Motoba, H. Bandō, and K. Ikeda, Prog. Theor. Phys. **70**, 189 (1983).
  - [8] E. Hiyama, M. Kamimura, K. Miyazaki, and T. Motoba, Phys. Rev. C **59**, 2351 (1999).
  - [9] H. Bando, T. Motoba and J. Žofka, Int. J. Mod. Phys. **A 5**, 4021 (1990).
  - [10] E. Hiyama, Y. Kino, and M. Kamimura, Prog. Part. Nucl. Phys. **51**, 223 (2003).
  - [11] E. Cravo, A. C. Fonseca, Y. Koike, Phys. Rev. C **66**, 014001 (2002).
  - [12] V. M. Suslov, I. Filikhin, and B. Vlahovic, J. Phys. G: Nucl. Part. Phys. **30**, 513 (2004).
  - [13] M. Shoen and Sonika, Phys. Rev. C **79**, 054321 (2009).
  - [14] R. Wirth, D. Gazda, P. Navratil, A. Calci, J. Langhammer, and R. Roth, Phys. Rev. Lett. **113**, 192502 (2014).
  - [15] M. Isaka, M. Kimura, A. Doté and A. Ohnishi, Phys. Rev. C **83**, 044323 (2011); **83**, 054304 (2011).
  - [16] M. Isaka, H. Homma, M. Kimura, A. Doté and A. Ohnishi, Phys. Rev. C **85**, 034303 (2012).
  - [17] M. Isaka, M. Kimura, A. Doté and A. Ohnishi, Phys. Rev. C **87**, 021304(R) (2013).
  - [18] H. Mei, K. Hagino, J. M. Yao, and T. Motoba, Phys. Rev. C **90**, 064302 (2014).
  - [19] H. Mei, K. Hagino, J. M. Yao, and T. Motoba, Phys. Rev. C **91**, 064305 (2015).
  - [20] Ji-Wei Cui, Xian-Rong Zhou, and Hans-Josef Schulze, Phys. Rev. C **91**, 054306 (2015).
  - [21] M. T. Win and K. Hagino, Phys. Rev. C **78**, 054311 (2008).
  - [22] B.-N. Lu, E.-G. Zhao, and S.-G. Zhou, Phys. Rev. C **84**, 014328 (2011).
  - [23] W. X. Xue, J. M. Yao, K. Hagino, Z. P. Li, H. Mei, and Y. Tanimura, Phys. Rev. C **91**, 024327 (2015).
  - [24] P. Ring and P. Schuck, The Nuclear Many-Body Problem (Springer-Verlag, Berlin, 1980).
  - [25] J. M. Yao, J. Meng, P. Ring, and D. Pena Arteaga, Phys. Rev. C **79**, 044312(2009).
  - [26] J. M. Yao, J. Meng, P. Ring, and D. Vretenar, Phys. Rev. C **81**, 044311(2010).
  - [27] T. Burvenich, D. G. Madland, J. A. Maruhn, and P.-G. Reinhard, Phys. Rev. C **65**, 044308 (2002).
  - [28] Y. Tanimura and K. Hagino, Phys. Rev. C **85**, 014306 (2012).
  - [29] M. Bender, K. Rutz, P.-G. Reinhard, and J. A. Maruhn, Eur. Phys. J. A **8**, **59** (2000).
  - [30] J.M. Yao, K. Hagino, Z.P. Li, J. Meng, and P. Ring, Phys. Rev. C **89**, 054306 (2014).
  - [31] J. Tauren and R. B. Firest, Evaluated Nuclear Structure Data File (ENSDF) [http://ie.lbl.gov/TOI2003/index.asp].
  - [32] H. Tamura *et al.*, Nucl. Phys. **A754**, 58c(2005).
  - [33] J.M. Yao, Z.P. Li, M. Thi Win, Y. Zhang, and J. Meng, Nucl. Phys. **A868-869**, 12 (2011).
  - [34] B. Bally, B. Avez, M. Bender, and P.-H. Heenen, Phys. Rev. Lett. **113**, 162501 (2014).